GPPS | JOURNAL

JOURNAL OF THE GLOBAL POWER AND PROPULSION SOCIETY
journal.gpps.global

# Mechanical design and rotordynamic analysis of the ORCHID turbine

**Special issue paper**

**Article history:**
**Submission date:** 29 March 2024
**Final revision date:** 23 July 2024
**Acceptance date:** 4 November 2024
**Publication date:** 22 May 2024

***Correspondence:**
MP: m.pini@tudelft.nl

**Peer review:**
Single blind



**Keywords:**
organic Rankine cycle; ORC; rotordynamics; squeeze film damper; gas seal; radial inflow turbine

**Citation:**
Majer M., Chatterton S., Dassi L., Gheller E., Pennacchi P. E. L. M., Colonna P., and Pini M. (2025). Mechanical design and rotordynamic analysis of the ORCHID turbine. Journal of the Global Power and Propulsion Society. 9: 45–66.
https://doi.org/10.33737/jgpps/195567

Matteo Majer[1], Steven Chatterton[2], Ludovico Dassi[2], Edoardo Gheller[2], Paolo Emilio Lino Maria Pennacchi[2], Piero Colonna[1], Matteo Pini[1,*]

[1]*Propulsion and Power, Faculty of Aerospace Engineering, Delft University of Technology, Kluyverweg 1, 2629 HS, Delft, The Netherlands*
[2]*Department of Mechanical Engineering, Politecnico di Milano, Via Privata Giuseppe La Masa, 1, 20156 Milano, MI, Italy*

## Abstract

The ORCHID turbine is a laboratory single-stage 10 kW high-speed (~100 krpm) radial-inflow turbine for high-temperature/high-efficiency organic Rankine cycle (ORC) systems, designed at the Aerospace Propulsion and Power laboratory of Delft University of Technology. It will be installed within a test section of the organic Rankine cycle hybrid integrated device (ORCHID) facility, the setup for fundamental and applied studies on ORC technology currently in operation in the same lab. Experimental data from future measurement campaigns will be employed to validate design and performance prediction tools and to develop best practices for operating these unconventional machines, whose most notable features are the ultra-high expansion ratio (>40), highly supersonic flow in the stator (Ma > 2), and the large flow deflection within the impeller channels (>90). This article presents the mechanical design and the rotordynamic assessment of the ORCHID turbine rotor, and best practices for the numerical evaluation of the rotordynamic characteristics and stability of high-speed ORC turbine rotors. The emphasis is on three main aspects: i) the modeling and quantification of the damping characteristics of a squeeze film damper (SFD) cartridge for the selected turbocharger ball bearings supporting the turbine shaft; ii) the characterization of the stiffness and damping coefficients of a custom designed pocket gas seal, performed using 3D RANS simulations; iii) the analysis of linear elastic rotordynamic simulations using a finite beam element model of the turbine rotor. Results of the rotordynamic simulations show that the rotor would operate in the sub-critical regime with respect to the first bending mode. The influence of model parameters such as the rotor eccentricity and the orbit radius was included in the analysis by conducting a parametric study of the SFD fluid forces. The Campbell diagrams show that shaft bending frequencies are significantly affected by changes in the SFD dynamic response depending on the rotational speed. The influence of the stiffness of rolling bearing elements and of the destabilizing forces due to the impeller and gas seal cross-coupled stiffness was also evaluated. The rigidity of the rolling elements slightly affects the shaft bending mode, while large values of the destabilizing forces cause a rotordynamic instability of the first rigid mode.

## Introduction

Organic Rankine cycle (ORC) power plants for the conversion of thermal energy into electricity at temperatures ranging from ≈120 °C to >500 °C and with a power capacity from few to tens MW are commercially available and employed to obtain renewable electricity from

geothermal reservoirs, industrial waste heat and the combustion of biomass. The expander is most often a high-efficiency multistage axial turbine, which has reached technological maturity. The commercial potential for smaller capacity ORC power plants is arguably very large, and ORC systems generating hundreds of kW of electricity and adopting either a radial-inflow turbine or a volumetric scroll expander have more recently been deployed. Turbines are an attractive technical solution, however, even with the selection of a suitable working fluid, the isentropic efficiency of small turboexpanders is bound to be negatively affected by scaling effects. Economic and technical complexity constraints often drive the choice of a single-stage radial-inflow turbine. Small-capacity ORC power plants available on the market feature relatively low thermal efficiency because volumetric machines cannot be designed for expansion ratios in excess of approximately 7, while, as far as turbines are concerned, the expansion ratio is also limited to similar values in order to avoid supersonic flows. The limitation of the expansion ratio implies a relatively low value of the expander inlet temperature ($\approx 150 - 170°C$). For a more extensive treatment of these aspects, see the review article of Colonna et al. (2015). The relatively low thermal efficiency of these systems often negatively affects their economic viability.

Scarce public technical information is available on low-temperature and low-capacity commercial ORC power plants. A U.S. company (Calnetix Technologies, n.d.) developed a system based on a hermetic assembly containing a radial-inflow turbine and permanent magnet generator on the same shaft supported by magnetic bearings (Yuksek and Mirmobin, 2015). The 125 kW unit was tested as a bottoming unit of a 31.6 MW marine vessel diesel generator recovering thermal energy from the 85°C water of the cooling jackets. The working fluid was R245fa, the expander pressure ratio was small – about 3.6 at the design point – and the measured isentropic efficiency at the nominal rotational speed of 16.5 krpm was 89.1%. Another U.S. company (Concepts NREC, n.d.) developed a 250 kW fully sealed ORC turbogenerator unit (Bella et al., 2015) also featuring magnetic bearings and operating with R245fa as working fluid. The proposed application was the conversion of thermal energy from the condensing steam at approximately 140°C typical of many industrial processes. The 3-stage axial impulse turbine ran at 20 krpm with a maximum pressure ratio of 7. The expander efficiency was not determined, but during the development tests the overall conversion efficiency of the ORC power plant was in excess of 12% at the maximum turbine inlet pressure of 19.7 bar. Also several European companies from France (Enogia, n.d.), Germany (Orcan Energy, n.d.), Spain (Rank, n.d.), Italy (Zuccato Energy, n.d.) and Sweden (Climeon, n.d.) have commercialized low-temperature small-capacity ORC power plants, however no public detailed technical information is available.

The market potential of high-temperature/high-efficiency ORC systems with a power output from few kW to several hundreds kW is arguably very large and financial viability would greatly improve because of the higher conversion efficiency of the system, which in turn lowers the initial investment, which largely depends on the cost of the heat transfer surfaces of the heat exchangers. Applications include waste heat recovery from engines (gas turbines, internal combustion engines, and in the future high-temperature fuel cells) both stationary and propulsive (automotive, naval, and in the future possibly aeronautical), and industrial waste heat recovery. In case of high-temperature small-capacity ORC power plants, volumetric expanders cannot be realized due to the excessively large expansion ratio and a radial inflow turbine is arguably the best type of expander. However, suitable working fluids are made of very complex molecules, therefore the speed of sound of the expanding organic vapor is of the order of tens m/s and the flow within a single-stage radial inflow turbine is bound to be highly supersonic. Its design is thus challenging, both from the fluid dynamic point of view and because of many other aspects related to high rotational speed, sealing and bearings technology, and rotordynamics.

To the knowledge of the authors, the only small-capacity high-temperature/high-efficiency ORC power plant on the market is commercialized by a Dutch company (Triogen, n.d.). The power capacity is approximately 150 kW and toluene was selected as the working fluid. The turbine, electrical generator and feed-pump are contained in a hermetically sealed assembly and liquid toluene is used to lubricate the bearings of the high-speed rotor. The turbine configuration is rather unique, in that the flow direction is radial both at the inlet and at the outlet, and it is equipped with a radial-to-axial diffuser which, however, negatively affects fluid dynamic performance. Harinck et al. (2013) reported that the expander is designed to operate at 25.8 krpm, the turbine inlet temperature is 317°C, the inlet pressure is 32.1 bar, the design back pressure is 0.292 bar, leading to a highly supersonic flow in the stator ($M \approx 2.5$) and a pressure ratio of about 110. The overall system efficiency is not reported, but it can be deduced that it is approximately double that of low-temperature systems of the same capacity.

Research on high-speed, supersonic radial-inflow turbines (sRIT) for high-temperature and small capacity ORC power plants is ongoing because these are unconventional machines for which validated design and operational guidelines are not available. The turbine is the technological core of the system and the overall conversion efficiency depends to a large extent on the efficiency of the expansion process. Several works, see, e.g., the articles

of De Servi et al. (2019), Cappiello and Tuccillo (2021), and Cappiello et al. (2022), describe the relevant flow features occurring in a sRIT and document best practices for their optimal thermo-fluid-dynamic design. For example, the numerical study of De Servi et al. (2019) shows that a sRIT may attain comparatively high fluid-dynamic efficiency ($\approx 80-85\%$), notwithstanding the shock-induced flow occurring in the stator. A systematic experimental verification of the performance of radial-inflow ORC turbines is however lacking and, accordingly, the validation of the methods and tools used for their design has not been performed yet.

The ORCHID turbine is a 10 kW, high-speed ($\approx 100$ krpm) and high-temperature laboratory sRIT for ORC, operating with hexamethyldisiloxane (siloxane MM) as the working fluid. This machine will be installed within a test section of the organic Rankine cycle hybrid integrated device (ORCHID) (Head, 2021), in operation at the Aerospace Propulsion and Power laboratory of Delft University of Technology. Data derived from future measurement campaigns will be used to (i) assess the achievable fluid dynamic performance of sRITs, (ii) validate the numerical tools employed for the design of these highly unconventional turbines, and (iii) develop experience and best practices for their optimal operation, including the thermal management of the bearings system.

Experimentally characterizing the fluid dynamic performance of ORC turbines requires a setup that ensures stable and safe operation of the machine from start-up up to nominal and off-design conditions. A few test benches for small-scale ORC turbines are or have been operational throughout Europe. A facility for testing a 10 kW axial-flow impulse turbine operating with ethanol as working fluid and featuring partial admission nozzles was designed and operated at the Turbomachinery and Fluid Dynamics Institute of Leibniz University in Hannover (Seume et al., 2017). The rotational velocity at the design point is 100 krpm, while the maximum stage pressure ratio of $\approx 50$ is achieved with an admission degree of 0.5. The turbine and electric generator rotors are supported on custom high-precision ball bearings. More recently, a test facility resembling an ORC turbogenerator powered by the exhaust gases of a diesel engine and featuring a 12 kW sRIT operating with octamethyltrisiloxane (siloxane MDM) as the working fluid has been commissioned at the Lappeenranta University of Technology (Uusitalo et al., 2020). The turbine stage was designed to rotate at 31.5 krpm, with a total-to-static pressure ratio of 112. The turbine, the main pump and the permanent magnet electric generator form a single assembly, similar to that described by Harinck et al. (2013). The turbogenerator shaft is supported on hydrodynamic bearings lubricated with liquid MDM. A 2.3 kW radial-inflow turbogenerator system was designed, commissioned and is operated at the Laboratory of Applied Mechanical Design of the École Polytechnique Fédérale de Lausanne (Rosset et al., 2021). The nominal speed is 100 krpm, the working fluid is R245fa and the turbine features a rotor supported on custom designed gas-lubricated bearings, allowing lower drag torque compared to liquid-lubricated bearings, and offering an efficient oil-free solution for low power capacity applications. Other laboratory facilities include those documented by Klonowicz et al. (2014), Kang (2016), and Weiß (2018), showcasing the increasing interest for small-scale ORC technology worldwide.

This article presents the layout of the ORCHID turbine rotor and documents the numerical methodology developed for performing the rotordynamic analysis of the assembly. A pocket gas seal (PGS) was designed for secondary flows management and its rotor dynamic characteristics modeled based on results of RANS computations. The rotordynamic coefficients of the squeeze-film-damper (SFD) cartridge were computed by numerical integration of the Reynolds equation, which was used to model the oil-film flow. A sensitivity analysis of the dynamic stability characteristics of the turbine rotor to some of the design parameters was also carried out.

## Turbine test-rig

The ORCHID is a unique closed loop test-rig capable of delivering superheated or supercritical vapor of siloxane MM up to 25 bar and 300°C, and with a maximum mass flow rate of $\sim 1.5$ kg s$^{-1}$ (Head, 2021). The aerothermal design of the ORCHID turbine was initially performed using meanline models, and then improved with RANS-based shape optimization (De Servi et al., 2019). The off-design fluid dynamic performance was also characterized by means of flow simulations, and an efficiency decay of up to 5 percentage points at part load was estimated. Cappiello et al. (2022) further optimized the fluid dynamic design of both the stator and the rotor by means of parametric analyses based on unsteady RANS, taking into account in-house manufacturing capabilities. The main geometrical characteristics, nominal operating conditions and estimated fluid dynamic performance associated with the current design are summarized in Table 1.

To determine the rotordynamic coefficients and forces required by the rotordynamic model of the powertrain, the fluid dynamic performance of the stage in the whole operating envelope was characterized by means of single-passage RANS simulations, using a commercial solver (Ansys Inc., 2022). Figure 1 shows the isentropic expansion processes for four different turbine pressure ratios in the reduced temperature-entropy diagram of siloxane

Table 1. Main design specifications of the ORCHID turbine.

| Geometry | | Nominal operating conditions | | Performance | |
|---|---|---|---|---|---|
| Impeller inlet radius | 25.75 mm | Total inlet pressure | 18.1 bar | Net power | 10.4 kW |
| Exducer hub radius | 8.2 mm | Static outlet pressure | 0.44 bar | Axial thrust | 132 N |
| Impeller inlet blade height | 2 mm | Total inlet temperature | 300°C | Total-total efficiency | 85.1% |
| Exducer blade height | 12.3 mm | Rotational speed | 98.1 krpm | Total-static efficiency | 81.2% |
| Impeller axial length | 10.2 mm | Massflow rate | 132 g $s^{-1}$ | | |
| Impeller inlet blade angle | 45° | Total-static expansion ratio | 41.1 | | |
| Impeller exit blade angle | −57° | | | | |
| Stator outlet blade angle | 80° | | | | |

MM. Four values of the turbine inlet pressure, corresponding to those of the isentropes A, B, C, and D in the figure – respectively 10.9 bar, 14.5 bar, 18.1 bar, and 23.5 bar – were chosen, and three different values of the rotational speed were considered, namely 80, 98.1, and 120 krpm. Thus, a total of 12 RANS simulations was carried out. The computational domain is the same as that adopted in the simulations reported by Cappiello et al. (2022). The mesh comprises a total of about 4 million cells, a grid size which was shown to guarantee mesh-independent results. A central difference scheme (CDS) was used for discretizing the advection terms to obtain a second order accurate solution, while the shear stress transport (SST $k-\omega$) model was employed for

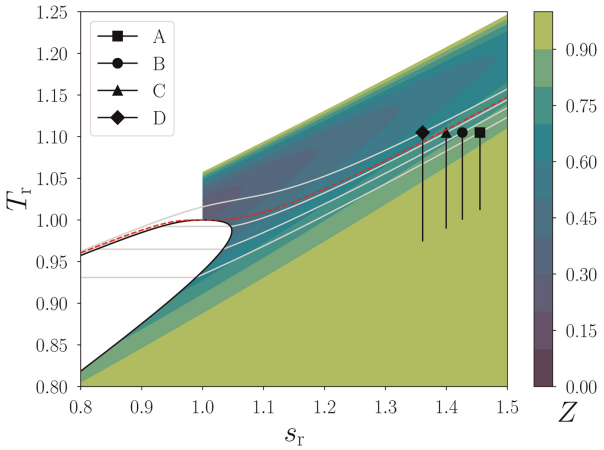


Figure 1. Isentropic (or ideal) turbine expansion processes (A–D) in the reduced temperature-entropy diagram of siloxane MM. The reduced temperature and entropy are defined as $T_r = T/T_{cr}$ and $s_r = s/s_{cr}$, where the subscript $cr$ refers to the vapor liquid critical point. The diagram reports also the colored contours of the compressibility factor $Z$ as an indication of the nonideality of the thermodynamic properties of the working fluid. The red dashed line indicates the critical isobar. These four turbine inlet conditions were chosen for the fluid dynamic characterization of the turbine in off-design operating conditions. The outlet static pressure of 0.44 bar is assumed the same for all the expansion processes.

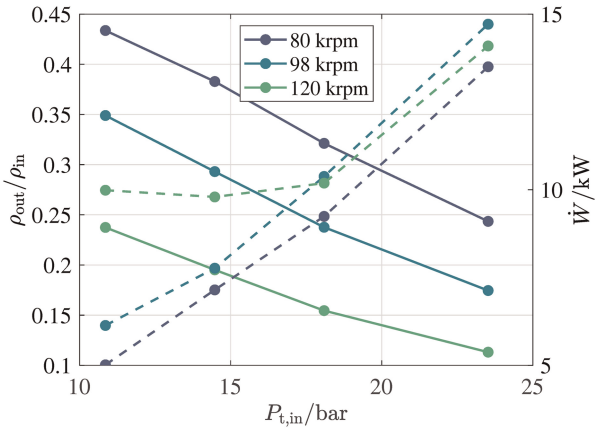


Figure 2. Density ratio across the impeller (solid lines) and stage net power (dashed lines) as a function of the stage inlet total pressure for three rotational speeds. The values are calculated using the results of the RANS simulations.

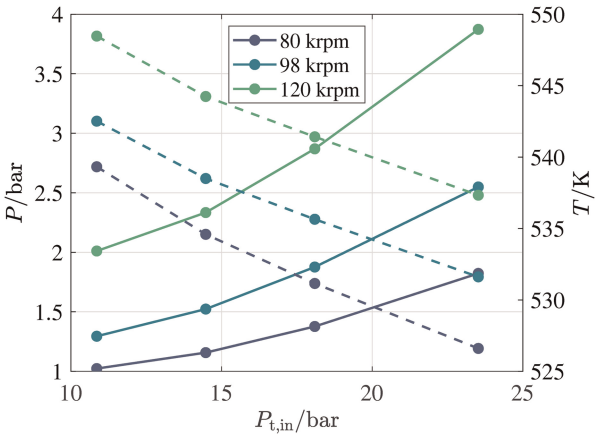


Figure 3. Impeller inlet static pressure (solid lines) and temperature (dashed lines) as a function of the stage inlet total pressure for three rotational speeds. The values are calculated using the results of the RANS simulations.

the turbulence closure, discretized using a hybrid scheme (Barth and Jespersen, 1989). The stage net power $\dot{W}$, the density ratio across the impeller $\rho_{out}/\rho_{in}$, and the impeller inlet static pressure $P$ and temperature $T$ obtained from CFD simulations are plotted in Figures 2 and 3 as a function of the stage inlet total pressure $P_{t,in}$, and for selected rotational speeds. With reference to Figure 2, one can notice that the net turbine power peaks for $P_{t,in} = 23.5$ bar with the turbine rotational speed equal to the design value of 98.1 krpm, due to the larger fluid-dynamic losses occurring if the turbine operates at 120 krpm with inlet pressures above 18.1 bar.

## Preliminary mechanical design

Key requirements of a turbine test-rig for research purposes are the possibility to test at different speeds and thermodynamic conditions, to obtain accurate measurements of all quantities relevant to performance characterization, to guarantee robust control of start-ups and shut-downs, and to be modular to ease the inspection and assembly of components.

Three main technical aspects were considered in the conceptual design phase:

1. The turbine arrangement (straddled or overhung rotor).
2. The type of bearings (gas-foil, rolling element – REB – and active magnetic bearings).
3. The sealing arrangement, closely linked to the bearings type and turbine configuration.

Figure 4a shows the straddled rotor configuration, with the turbine wheel placed within two bearings. Figure 4b instead shows an example of overhung impeller configuration, with the wheel mounted outboard on the right-hand side. Straddled rotors are arguably more robust and lead to smaller shaft deflections, but the bearings on each side of the wheel lead to a more complex assembly. Conversely, overhung impellers result in a less complex and more easily accessible assembly, but the rotordynamics is arguably more challenging.

The use of ceramic ball bearings for a turbine of this type provides two main advantages over competing technologies. Firstly, they can withstand substantially higher loads than gas-foil bearings, offering a robust solution

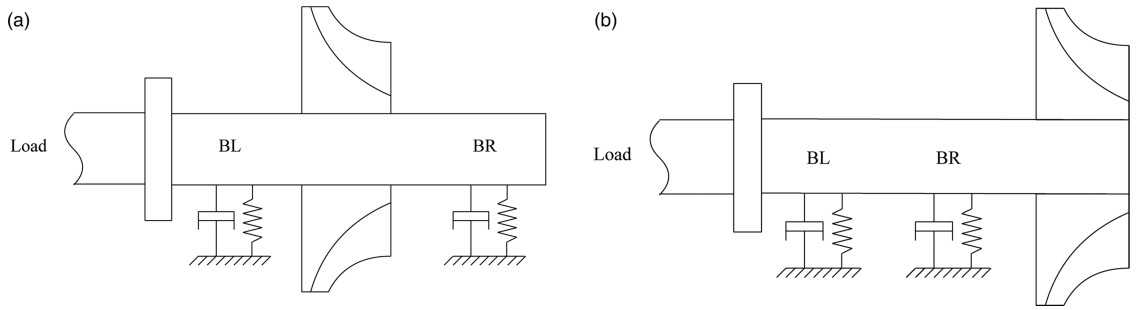


Figure 4. Rotor configuration concepts. (a) Straddled impeller, and (b) overhung impeller.

for a wide range of operating conditions. Secondly, thanks to the widespread use of REB in a plethora of applications, they are available off-the-shelf and can be readily implemented within a new design. Recent trends in the design of turbocharger systems show that rolling element bearings can be preferable for compact, mobile systems such as automotive turbochargers (Schweitzer and Adleff, 2006), providing, even at high speeds, long term durability with lubrication and mechanical losses comparable to those of noncontact bearings (Nguyen-Schäfer, 2012).

Albeit the use of REB simplifies the assembly design, the need for lubrication poses additional challenges compared to gas-foil bearings. The oil contamination of the working fluid can severely impact the performance and integrity of the entire rig, causing mechanical damage to the rotating components due to erosion. Moreover, leaked oil accumulates and forms sludge, increasing the risk of thermal decomposition of the working fluid whenever in contact with hot spots in the rig. Therefore, the choice of a proper sealing technology is key to ensure safe and reliable operation of rotors supported on oil lubricated ball bearings. To prevent lubricant leakages, a common strategy adopted for large steam power plants is to use dry-gas seals (Forsthoffer, 2011), employing an inert gas like nitrogen as a barrier between the two fluid flows. As an alternative, contact seals capable of guaranteeing almost no oil leak are commonly adopted in low temperature and low speed applications. The advantage of the dry-gas solution is the absence of contact parts between the stationary and the rotating components, but this comes at the cost of a more complex rotor design. The use of dry-gas as a barrier requires also more components and more complex control strategies. Conversely, contact seals lead to a simpler and more compact assembly. The rotational speed and maximum operating temperature of ORC turbines is lower than those of turbochargers, therefore inexpensive contact seals can be used (such as those of the stationary lip seal type). Advancement in the development of low friction materials and temperature resistant coatings enables state-of-art contact seals to operate at peripheral speeds of up to 100 $ms^{-1}$ in combination with temperatures in excess of 250°C. Therefore, polytetrafluoroethylene (PTFE) based lip seals were deemed appropriate for the ORCHID turbine, and the suitability of this choice was also confirmed by a manufacturer.

The conceptual layout of the rotor configuration obtained as a result of an iterative design process is shown in Figure 5. The rotor includes a shaft (A), a turbocharger cartridge (B), a turbine wheel (C), and a coupling flange (D). A lock-nut on the left side of the bearing inner raceway (E) is used to regulate the mounted-end-play of the rolling elements by adjusting the preload. The cartridge pushes axially against a stainless steel thin-disk (F), whose function is that of moving the oil outwards and to the main drain bore in the center of the assembly, through a cavity realized in the casing and extending 50° circumferentially (visible on the right of the main oil drain bore). Stationary parts include two off-the-shelf contact lip seals (G on the impeller side or hot side and H on the coupling side) to contain the oil within the turbine casing, and a noncontact gas seal (J) which was designed in-house.

## Rotordynamic modeling

The computation of the so-called rotordynamic coefficients, i.e., the stiffness and damping coefficients, is necessary to perform the assessment of the dynamic stability and characteristics of the rotor. External forces acting on the rotor-shaft due to the presence of the bearing cartridge SFD, the gas seal and the turbine impeller have been modeled and used to determine the system lateral vibrations through the stiffness and damping coefficients. The modeling approach is described in detail in the following.

### Characterization of the dynamic response of the squeeze-film damper

The main function of the bearing cartridge is to support the powertrain and to transfer the loads to the structure. A three-dimensional representation of the bearing cartridge is shown in Figure 6. The cartridge inner ring, having a bore diameter of 10 mm, is fitted to the turbine shaft, while the outer ring has a radial clearance fit of 50 µm with the casing. The cartridge outer diameter is 29 mm and the overall length is 62 mm. Two rows of rolling elements are interposed between the two rings. The outer ring is axially locked in the casing using a snap-ring (item K in detail L of Figure 5), while a rectangular slot and pin system (L) is used as a circumferential lock. The two regions highlighted in red in Figure 6 act as squeeze-film-dampers. Both feature an axial length $L$ of 9 mm. The clearance fit ensures that, as a result of lateral motion of the powertrain, the outer ring squeezes the oil-film in the gap, resulting in film pressurization and system damping. The lubricant selected for the application is an ISO VG 32 oil. The oil enters the SFD lands from the supply grooves shown in Figure 5 and is discharged at the other extremity. The bearing cartridge must be operated with a relatively large oil flow rate to cool down the rolling element bearings during their operation. Therefore, the bearing cartridge is considered to be

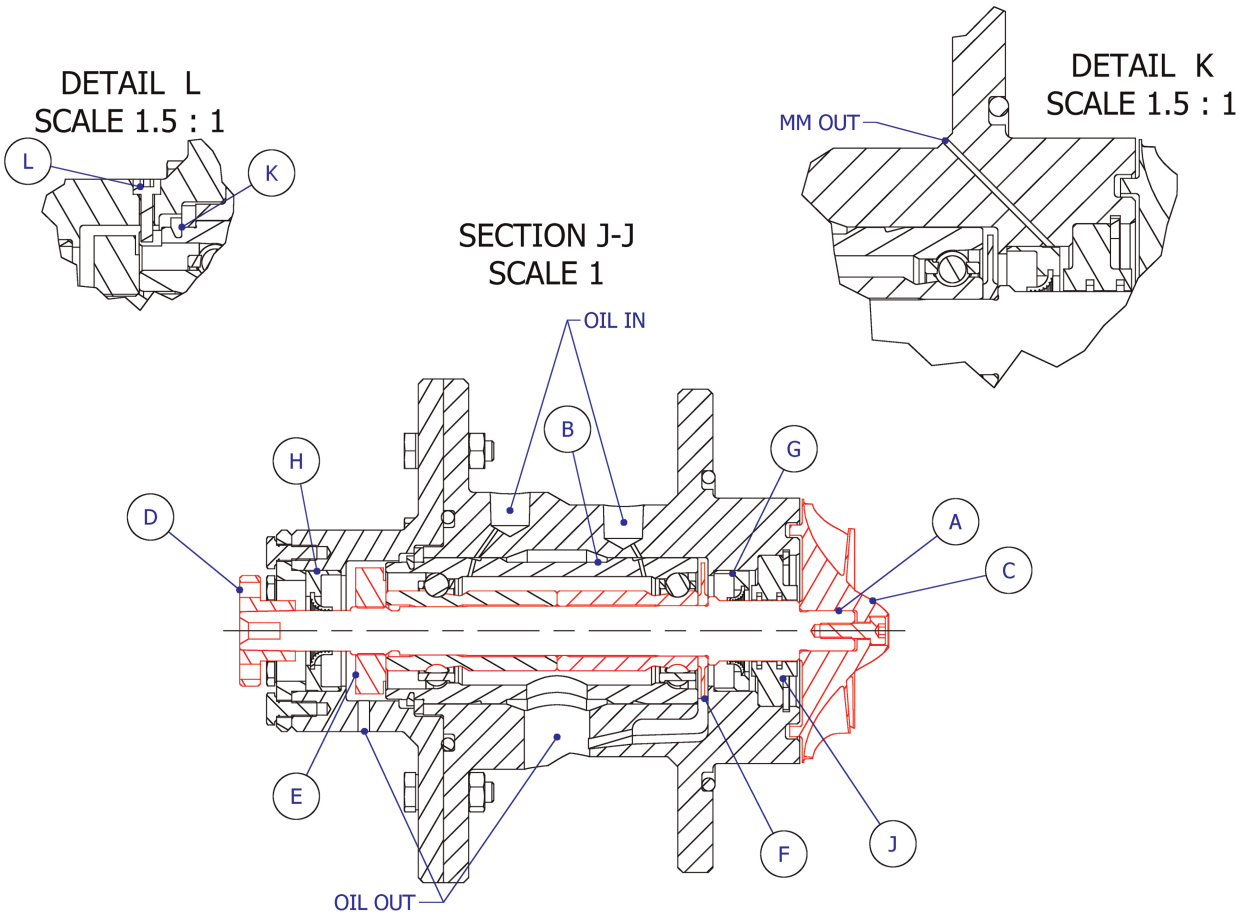


Figure 5. ORCHID turbine cross-section, showing the main components and details of the oil delivery system. Red lines indicate the rotating parts. Details K and L are viewed from a cross-section rotated 90° with respect to J-J section.

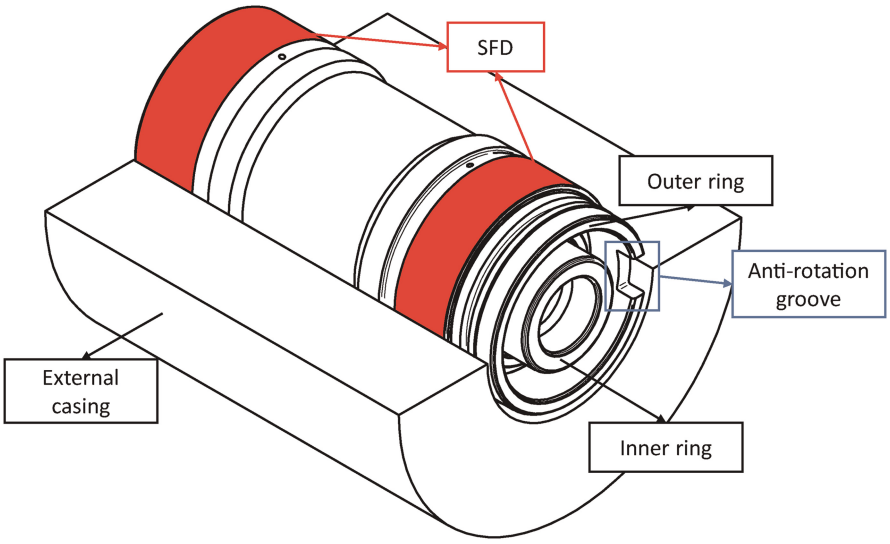


Figure 6. Housing cut-off revealing the rolling element bearing cartridge. The red areas indicate the SFD lands.

operated in an oil bath and air ingestion is neglected. As a first approximation, ambient pressure is assumed as boundary condition at the two axial ends of the SFD for the investigation of this preliminary design.

The Reynolds equation describes the dynamic pressure generation in the oil film of the SFD. Considering the SFD radial clearance $g = 50$ μm, the synchronous excitation $\omega$ at the maximum machine operating speed, and

the oil density $\rho = 852.7\ \mathrm{kgm}^{-3}$ and viscosity $\mu = 16.3 \cdot 10^{-3}$ Pa s at 50°C, the squeeze Reynolds number $\mathrm{Re}_s = \rho\omega g^2/\mu < 2$ throughout the entire range of considered rotational speeds. Previous studies on the development of dynamic forces in SFD (San Andres and Vance, 1987; Delgado and San Andres, 2010) have shown that fluid inertia has a marginal influence on the generation of the pressure field if $\mathrm{Re} \leq 10$, and it was therefore neglected in this work.

The computer program developed and documented by Gheller et al. (2022) was modified to model the oil flow squeezing within the SFD. The program performs the numerical integration of the Reynolds equation

$$\frac{\partial}{R\partial\theta}\left(\frac{\beta h^3}{12\mu}\frac{\partial \eta}{R\partial\theta}\right) + \frac{\partial}{\partial z}\left(\frac{\beta h^3}{12\mu}\frac{\partial \eta}{\partial z}\right) = \frac{\partial}{\partial t}(\eta - \xi) + \rho_c \frac{\partial h}{\partial t}, \tag{1}$$

where $\theta$, $z$ and $R$ are the tangential, axial and radial coordinates, $h$ is the oil-film thickness, $P$ is the oil pressure, and $\beta$ is the fluid bulk modulus. $\eta$ and $\xi$ are a so-called complementarity pair, thus variables introduced to linearize the change of fluid properties across phase interfaces. Due to the high operating speed of the turbine and the small radial gap of the SFD, oil cavitation may occur (Zeidan and Vance, 1990). The motion of the cartridge towards the casing causes the oil-film pressure to rise locally due to the squeezing, while on the opposite side of the cartridge the oil-film pressure decreases as the cartridge moves away from the external casing. As a result, the liquid is forced to move circumferentially away from the location of minimum film thickness. Thus, at high pressures the oil flow velocity can be such that its static pressure drops below the saturation pressure and cavitation bubbles form in the film (Nguyen-Schäfer, 2012). The application of the linear complementarity problem (LCP) included in Equation 1 to model cavitation in SFD has been previously demonstrated by Fan and Behdinan (2017).

The powertrain design does not include a centering element for the external ring of the bearing cartridge. Thus, when the machine is not running the external ring of the bearing cartridge rests on the casing. As the rotational speed increases, the rotor excitation (e.g., residual unbalance forces) drives the outer ring far from the casing and generates the squeeze responsible for the oil pressurization. The ORCHID turbine is designed to operate at constant speed, and once the operating speed is reached, the motion of the outer ring reaches the so-called limit cycle. Full characterization of the limit cycle would require a transient simulation of the startup. At the level of preliminary analysis, a parametric study of the rotordynamic performance considering circular orbits and a vertical static eccentricity is conducted. Thus, the relation describing the oil-film thickness distribution over time and space in the tangential direction can be expressed as

$$h(\theta, t) = g - (e\cos\omega t + e_s\cos\theta_s)\cos\theta - (e\sin\omega t + e_s\sin\theta_s)\sin\theta, \tag{2}$$

where $h$ is a function of the dynamic eccentricity, which in this work has been included using circular orbits of radius $e$ in an orthogonal plane, and of the static eccentricity $e_s$ with phase $\theta_s$.

Equation 1 is numerically solved to compute the pressure distribution in the SFD for several shaft positions within a circular orbit. The orbit-based dynamic force coefficients are calculated as suggested by San Andres and Jeung (2016). Figure 7 illustrates the circumferential distribution of the pressure evaluated at the SFD midplane $z/L_{\mathrm{SFD}} = 0.5$ and for increasing rotational speed, considering a relative orbit radius of $e_r = e/g = 0.25$ and a vibration frequency that is synchronous with the rotor rotational speed. As expected, only a fraction of the SFD circumferential extension provides a significant reaction force during operation. This is confirmed by the relatively narrow region where high pressure in the oil-film is developed, whereas the remaining portion of the oil-film undergoes cavitation – i.e., the region where the pressure profiles becomes a flat line – with a pressure of 1,000 Pa. The same figure also shows that increasing rotational speeds have a significant impact on the generation of oil-film pressure, highlighted by the increase in magnitude of the pressure peak and by the reduction of the region unaffected by cavitation along the circumferential direction.

The impact of the rotor eccentricity and of the orbit radius on the SFD direct damping and stiffness coefficients is displayed in Figure 8 for the design rotor speed of 100 krpm. The two maps displayed on the left of Figure 8 show the variations of the direct stiffness coefficients, while the two on the right show the direct damping coefficients. Several SFD orbits have been simulated with relative static eccentricity ranging from 0 (centered orbit) to 90% of the available radial clearance in the downward vertical direction. A purely vertical and downward shift of the center of rotation is a realistic condition during operation, in which the rotor is off-centered under the action of its own weight. The lower value of the orbit radius is limited to the 5% of the radial clearance. The maximum value of the orbit radius is linearly varied as a function of the eccentricity, up to 90% of the radial clearance for a centered orbit and to 5% for a 90% eccentric orbit.

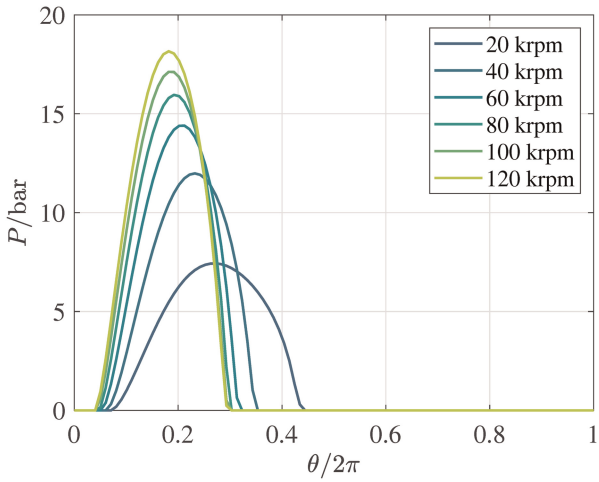


Figure 7. SFD pressure profile at midplane for $e_r = 0.25$ calculated with equation 1.

Considering the left contours of Figure 8, one can observe that the SFD generates increasing direct stiffness coefficients as either the orbit radius and the rotor eccentricity become larger. A squeezed oil-film interested by partial cavitation does not only generate a damping force, but also a centering force (Vance, 1998): the oil-film thus acts as a centering spring. With reference to the right contours, the damping provided by the SFD increases for either small and large orbit radii. This is due to the fact that, despite the portion of oil-film undergoing cavitation increases with larger orbits, the maximum pressure in the film also increases and compensates the detrimental effect of cavitation. As expected, the static eccentricity has a larger impact on $k_{yy}$ and $c_{yy}$, since a vertical static eccentricity is considered and the outer ring operates with a reduced clearance in that direction. $k_{xx}$ and $c_{xx}$ are instead significantly less affected by the static eccentricity. For the cases of null static eccentricity, centered circular orbits lead to equal direct force coefficients and thus $c_{xx} = c_{yy}$, and $k_{xx} = k_{yy}$. Since the static eccentricity considered is purely along the vertical direction, the calculated cross-coupled force coefficients are negligible.

Previous study on oil cavitation in SFD (Zeidan and Vance, 1990) showed that once the so-called bubbly region is reached, oil pressure and thus damping characteristics stabilize even with a further increase of the vibration frequency. Moreover, larger SFD vibrations (thus larger orbits) cause larger pressure differences within the oil-film (San Andres and Jeung, 2016), causing larger portions of the film to cavitate. The dynamic response of

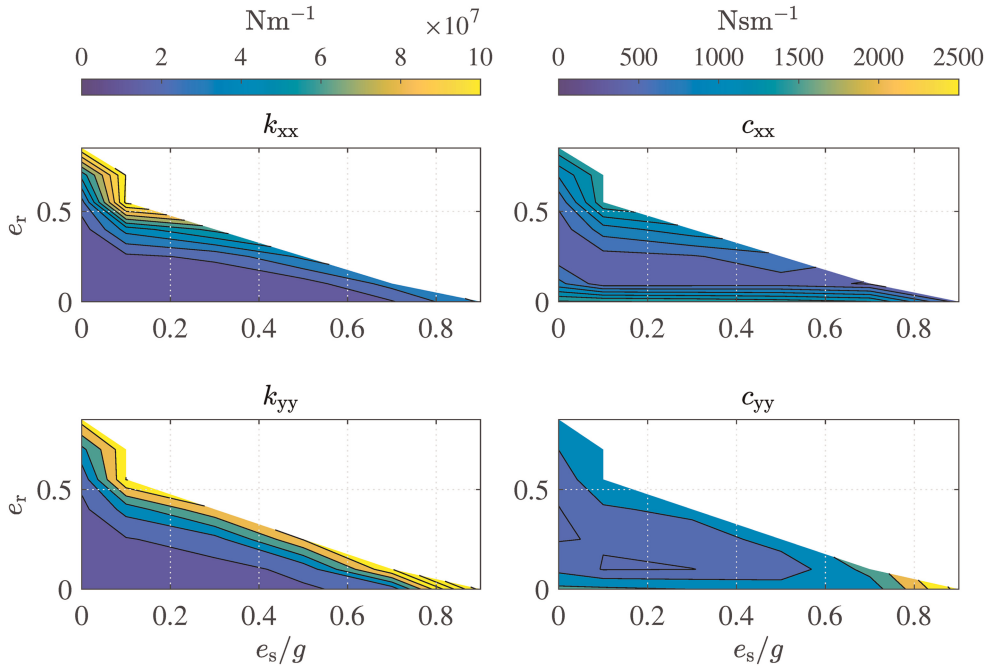


Figure 8. SFD stiffness and damping direct coefficients at 100 krpm as a function of the relative rotor eccentricity ($e_s/g$) and of the relative orbit radius ($e_r$).

the SFD has been analyzed for synchronous excitation with the rotational speed of the rotor. The evolution of the SFD dynamic coefficients with the rotational speed $n$ is shown in Figure 9. Grey bands refer to the variation of coefficients with relative static eccentricities between 0 and 90%, while the colored bands refer to the variation of rotordynamic coefficients with increasing relative orbit radii for the case of a centered rotor. The mean values as a function of rotor speed used in the rotordynamic analysis are shown in the figure by means of a dashed black line.

## Design and characterization of a pocket gas seal

The hot side lip seal chosen for this application, i.e., G in Figure 5, can seal up to 5 bar of pressure differential between the bearing cavity and the outside environment. Vice versa, even small pressure gradients would cause the entrainment of gas in the bearing cavity with negative consequences for bearing life. Thus, to prevent pressure build up on the impeller side of the lip seal, a gas seal was introduced between the impeller and the lip seal itself to cause a pressure drop of the pressurized siloxane behind the impeller disk. The selection of the seal type was performed by comparing the rotordynamic coefficients obtained with different types of seals. In particular, for the ORCHID rotor operating conditions and geometry, the calculation of the stiffness and damping coefficients was based on the experimental data for labyrinth seals (LS), fully partitioned pocket damper seals (FPDS) and honeycomb seals (HS) provided by Ertas et al. (2012), normalized following the approach of Childs et al. (1989). The calculation requires the shaft rotational speed, the seal type, length, diameter, the radial clearance and the pressure ratio across the seal. The pressure ratio across the gas seal of $\sim$1.7 was obtained as the ratio between the turbine stator outlet pressure, and the maximum allowable pressure on the impeller side of the lip seal to avoid siloxane leakage in the bearing cavity. In this application, since the bearing cavity pressure is assumed equal to the ambient pressure, the maximum allowable downstream pressure of the gas seal is also equal to the ambient pressure. A seal length of 9 mm was chosen, which was selected as a trade-off between a sufficient number of pocket rows to limit the leakage and the manufacturing constraint deriving from the minimum

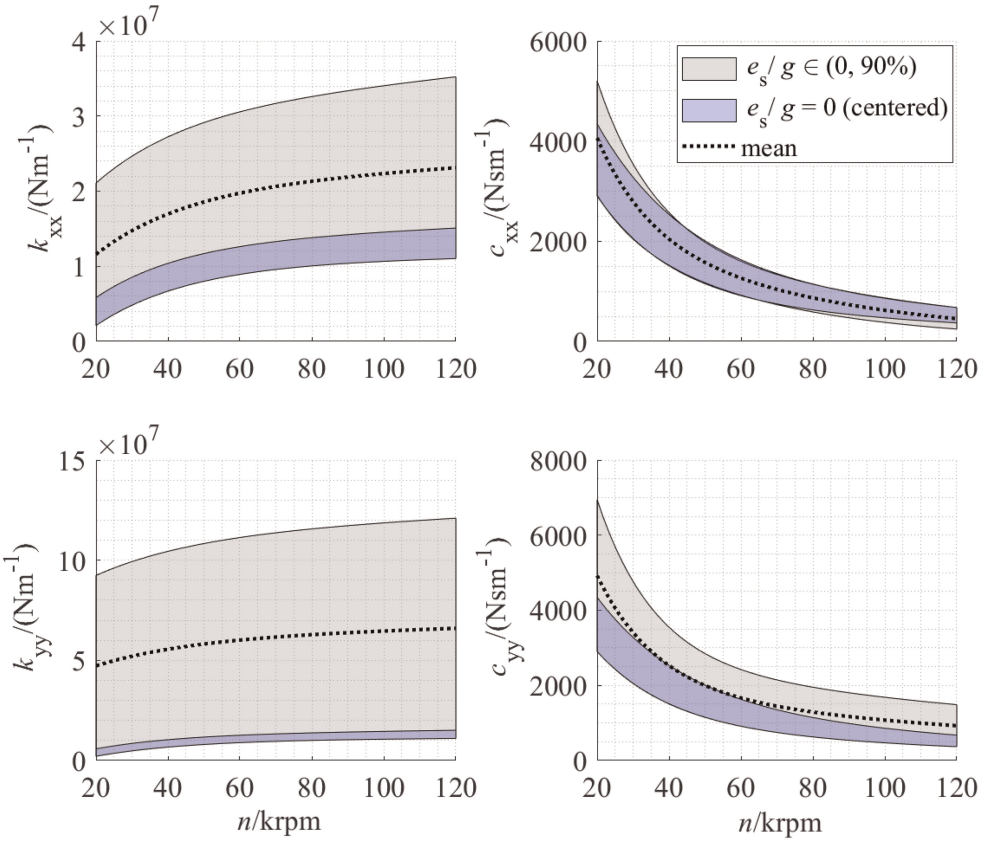


Figure 9. SFD dynamic coefficient range for several values of orbit radius and eccentricity. The gray shaded bands are used to account for the variation of coefficients with relative static eccentricities between 0 and 90%, while the colored bands refer to the variation of rotordynamic coefficients with increasing relative orbit radii between 5 and 85% assuming a centered rotor. The dashed back lines indicate the average value.

material thickness separating adjacent pocket rows, while maintaining acceptable overhang of the impeller wheel. The internal diameter of 12.25 mm of the gas seal was selected to leave enough radial clearance – corresponding to 125 μm in the *as-built* state of the parts – between the shaft outer surface and the seal inner surface. The value of clearance was informed by a radial stack-up analysis of the components, considering the effect of centrifugal stress, Poisson deformation, thermal expansion, and the contribution of rigid lateral vibrations of the rotor about its barycenter. The maximum shaft diameter of 12 mm was chosen to keep the shaft surface speed at off-design conditions below 100 $ms^{-1}$, as prescribed by the presence of the lip seal. The dynamic coefficients computed for three seal types are reported in Table 2. The results of the calculation revealed that the LS provides the lowest effective damping – defined as $c_{eff} = (c - k/\omega)$, where $\omega$ is the shaft angular speed in rad $s^{-1}$ – with the FPDS achieving similar damping performance as the HS.

To minimize the destabilizing effects associated to traditional labyrinth seals and to avoid the geometrical complexity of FPDS and HS type seals, a pocket gas seal type (PGS) was designed. The PGS is essentially a labyrinth seal with internal swirl breakers, providing additional damping and dynamic stability as in FPDS and HS. The component was designed as a single-body, hollow disk made of stainless steel (AISI 316) with four rows of pockets acting as labyrinths. Adjacent rows of pockets were shifted relatively to each other to avoid preferential paths for the leaking vapor. The pockets extend 50° along the circumferential direction and 1 mm along the axial one to guarantee feasibility with additive manufacturing methods.

The pocket seal geometry and its relevant dimensions are illustrated in Figure 10. Additive manufacturing was chosen as production process for this component to allow geometrical freedom and to make the manufacturing cost-effective. Thin walls between adjacent pockets are arguably the most critical component feature from a manufacturing standpoint, therefore their thickness was chosen according to standard design guidelines for 3D metal parts (Ewald and Schlattmann, 2018). Novel printing techniques such as metal binder jetting are effective for manufacturing complex geometries, without requiring additional material for supporting the overhanging regions of the part (Blunk and Seibel, 2023). Nevertheless, material finishing by means of conventional manufacturing techniques will still be required to achieve the small dimensional tolerance required at the inner diameter of the PGS.

RANS simulations of the flow within the PGS were carried out to estimate the leakage mass flow and the dynamic coefficients (i.e., stiffness and damping) at the nominal operating conditions of the rotor. A commercial CFD solver (Ansys Inc., 2021) was used for this study, and the computational domain displayed in Figure 11 was discretized using a hybrid approach comprising an unstructured mesh body and a structured layer near the walls. The domain was extended at the inlet and outlet of the PGS-shaft clearance gap as shown in the figure to prevent boundary conditions from influencing the flow solution inside the domain. The fluid domain geometry has been simplified to reduce the computational cost of the simulation, and because the objective of the analysis is to predict the flow motion within the clearance between the PGS and the shaft. Thermal deformation of the seal geometry due to temperature gradients has been neglected, as a result of the minimal temperature drop of just 3°C across the seal, which justifies the assumption of isothermal operation of the component. The presence of flow swirl at the inlet of the PGS was also disregarded, because a proper characterization of this quantity would require the complete modeling of the secondary flow passage behind the impeller disk. The additional modeling and computational efforts are deemed redundant given the low values of the dynamic coefficients of the seal. Moreover, the uncertainty of the PGS rotordynamic coefficients deriving from this simplification has been included in the form of a sensitivity analysis of rotor stability to the magnitude of cross-coupled stiffness terms.

The discretized computational domain comprised 5.1 million cells as a result of a mesh independence study. Local inflation was added at non-slip walls (i.e., shaft and PGS surfaces) to properly resolve the boundary layer,

Table 2. Comparison of dynamic coefficients for different seal types.

| Seal type | $k_{xx}/(Nm^{-1})$ | $k_{xy}/(Nm^{-1})$ | $c_{xx}/(Nsm^{-1})$ | $c_{eff}/(Nsm^{-1})$ |
|---|---|---|---|---|
| LS | 3,154 | 7,884 | 11 | 4 |
| FPDS | 15,768 | 18,922 | 39 | 26 |
| HS | 20,498 | 16,556 | 23 | 19 |

LS, Labyrinth Seal; FPDS, Fully-partitioned Pocket Damper Seal; and HS, Honeycomb Seal.

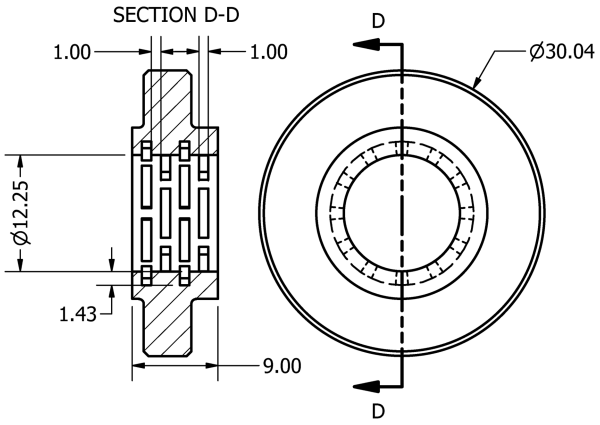


Figure 10. Geometry of the PGS showing the main dimensions in mm.

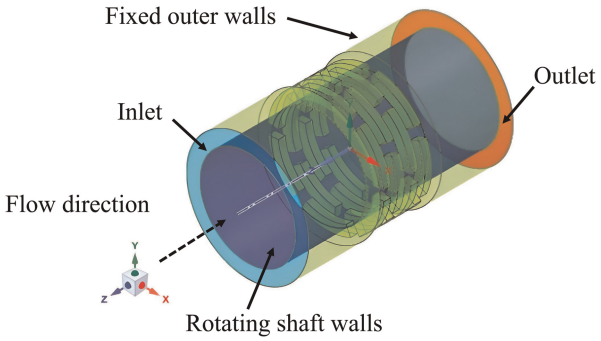


Figure 11. Computational domain used for the CFD flow simulations of the PGS. The employed boundary conditions are also indicated. The flow through the geometry of the gap between the shaft outer surface and the PGS inner surface is modeled.

while the dimension of the cells was adjusted in the clearance region to maintain the maximum $y^+_{max} < 10$. Total pressure and temperature were imposed at the inlet and static pressure at the outlet, whose values are reported in Table 3. The SST $k$-ω model was employed as turbulence closure and look-up tables generated using a multi-parameter equation of state (Huber et al., 2022) were used for computing the fluid properties. Flow simulations for shaft rotational speeds varying from 20 krpm to 100 krpm were carried out to investigate the impact of the gas seal on system stability at different speeds. A nominal radial gap between the inner seal and the shaft outer surface of 50 µm was imposed, which corresponds to the minimal residual clearance estimated for the parts during operation, and also leads to the largest dynamic forces.

The leakage mass flow rate of siloxane MM computed from CFD was compared with the predictions from an empirical method commonly employed in gas turbine engines (Ludwig, 1980), namely the Egli model of labyrinth seal flows (Egli, 1935). Figure 12 shows the comparison of the massflow rate through the PGS predicted by the Egli model and by the CFD as a function of radial clearance $c$. Despite the Egli model is rigorously valid for labyrinth seal geometries, the mass flow predicted by the two models is in close agreement and varies linearly with the increase in the radial clearance.

For the estimation of the rotordynamic coefficients, the forces in the horizontal and vertical directions acting on the shaft, $F_x$ and $F_y$, were calculated by integration of the pressure field on the shaft outer surface. The direct and cross-term stiffness and damping coefficients were calculated according to their definitions

$$k_{xx} = -\frac{F_x - F_{x_0}}{\Delta x}; \quad k_{xy} = -\frac{F_y - F_{y_0}}{\Delta x}; \quad c_{xx} = -\frac{F_x - F_{x_0}}{\Delta \dot{x}}; \quad c_{xy} = -\frac{F_y - F_{y_0}}{\Delta \dot{x}}, \tag{3}$$

where the denominators are the imposed displacements and displacement rates, whose magnitude was determined by means of a convergence study in which their value was varied until stiffness and damping coefficients

Table 3. Boundary conditions for gas seal CFD simulations.

| Quantity | Inlet | Outlet |
|---|---|---|
| $P_t$/bar | 1.7 | – |
| $T_t$/K | 534 | – |
| $P$/bar | – | 1.0 |
| $n$/krpm | 98.1 | |

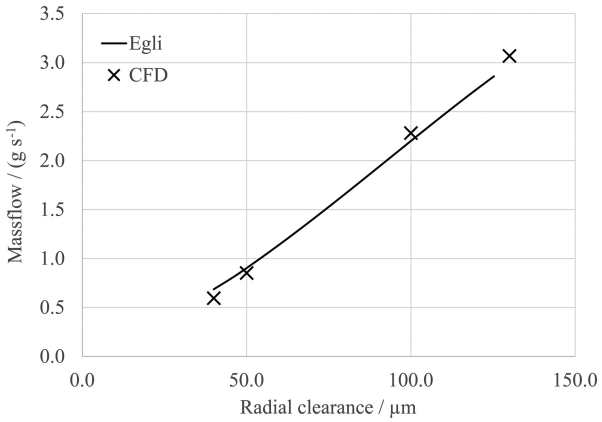


Figure 12. Leakage massflow rate through the PGS as a function of the radial clearance. Comparison between CFD results ( × ) against predictions with the Egli equation (solid line).

reached asymptotic values for small amplitude vibrations. $F_{x_0}$ and $F_{y_0}$ are the fluid dynamic forces with null shaft displacement. Figure 13 shows the computed stiffness (see 13a) and damping (see 13b) coefficients at varying rotational speed of the rotor shaft.

At low speed, direct stiffness coefficients are the responsible for most of the PGS stiffness, while the contribution of the cross-coupled stiffness is important only at higher rotational speeds. According to Ertas et al. (2012), seals are characterized by cross-coupled stiffness coefficients opposite in sign which can lead to rotor instability. This is also the case for the PGS considered in this work. The terms on the secondary diagonal of the stiffness matrix are of opposite sign, though their magnitude is similar, i.e., $|k_{xy}| \approx |k_{yx}|$. The magnitude of the generated damping coefficient is also relevant for the evaluation of stabilizing or destabilizing effects on the rotor. It is found, however, that the magnitude of all the damping terms is negligible.

The rotordynamic coefficients computed with the CFD model have been compared to those obtained using the empirical correlation by Ertas et al. (2012) for the honeycomb seal type. Even if the geometry is different, the empirical correlation provides results similar to those obtained with CFD, as reported in Table 4. The prediction of the cross-coupling stiffness by means of the two models differs by about 6.9%. The direct stiffness predicted by the empirical model is about 2.6% higher than the value computed using CFD. Recently, Delgado et al. (2022) conducted a similar CFD investigation to characterize the rotordynamic coefficients of a fully partitioned pocket damper seal (FPDS) and found that the direct stiffness terms computed via CFD are overpredicted if compared to experimental measurements. This result is relevant in that CFD can be used to attain conservative values of the stiffness terms related to the PGS.

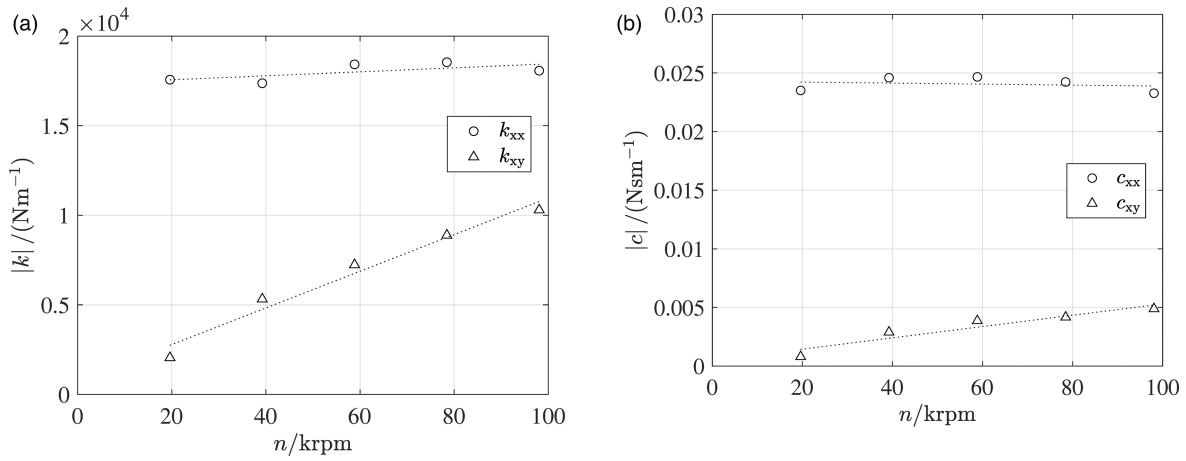


Figure 13. Stiffness (a) and damping (b) coefficients computed with CFD simulations. Dotted lines are linear fits used as input for the rotordynamic analysis. The symbols indicate direct ( ◯ ) and cross-coupled (△) coefficients.

Table 4. Comparison of seal dynamic coefficients calculated with CFD and with a simplified model.

| | $k_{xx}/(\mathrm{Nm}^{-1})$ | $k_{xy}/(\mathrm{Nm}^{-1})$ | $c_{xx}/(\mathrm{Nsm}^{-1})$ |
|---|---|---|---|
| CFD | 19,971 | 17,780 | 0.012 |
| HS from Table 2 | 20,498 | 16,556 | 23.652 |
| Deviation /[%] | 2.64 | −6.88 | – |

## Determination of the impeller fluid-structure interaction forces

Fluid-structure interaction (FSI) forces in fluid machines are often responsible for rotordynamic instabilities, potentially damaging the components and in some cases leading to catastrophic failure of the entire system. Unsteady flows in rotor-shroud clearances due to unsteady pressure fields and rotational eccentricities are responsible for the generation of non-axisymmetric pressure fields that cause forces perpendicular to the axis of rotation (Alford, 1965). San Andres (2023) performed an extensive review of the different methods to predict the magnitude of destabilizing forces due to this dynamic forcing using both semi-empirical methods, such as those of Alford (Alford, 1965) and Wachel (Wachel and von Nimitz, 1981), and more advanced methods based on CFD (Moore et al., 2010).

In this study, the destabilizing aerodynamic force coefficient has been predicted according to the Wachel formula (Wachel and von Nimitz, 1981), i.e., the standard method for radial expander-compressor systems (API, 2002). The model allows one to estimate the stiffness coefficient contributing to the systems lateral vibrations

$$k_{xy}^{\mathrm{aero}} = 9.55 \cdot \frac{\dot{W} \cdot B_c}{D \cdot b \cdot n} \cdot \frac{\rho_{\mathrm{out}}}{\rho_{\mathrm{in}}}, \tag{4}$$

where $\dot{W}$ is the mechanical power in $W$, $D$ and $b$ are the turbine wheel inlet diameter and inlet blade height in $m$, $n$ is the angular speed in rpm, and $\rho_{\mathrm{in}}/\rho_{\mathrm{out}}$ is the density ratio across the impeller. In the API 617 (API, 2002) standard, $B_c = 3$, and the value is obtained dividing by ten a fluid molecular weight of 30 kg kmol$^{-1}$, which is representative of light hydrocarbons used in industrial processes.

The destabilizing cross-term was computed for the different operating points of the turbine, using the fluid density ratio and the stage power determined by means of CFD simulations at different operating conditions and plotted in Figure 2. Solid lines in Figure 14 depict the values of $k_{xy}$ obtained from Equation 4 with $B_c = 3$ as function of the stage inlet total pressure and at different rotational speeds. The dashed lines were obtained computing $k_{xy}$ according to the same model but with a modified constant $B_c$ – equal to 16.234 considering that the molecular weight of siloxane MM is 162.34 kg kmol$^{-1}$ –, while the dotted lines were obtained using the correlation developed by Moore & Ransom (Moore et al., 2010) for centrifugal compressors, adapted to radial turbo expanders as suggested by other authors (Lerche et al., 2013; San Andres, 2023). The values of $k_{xy}$ obtained with the modified Wachel model, i.e., for $B_c = 16.234$, and the Moore & Ransom method are similar in magnitude, although the trends as a function of the stage inlet total pressure and rotational speed are qualitatively different. As highlighted by previous research on this topic (San Andres, 2023), a general consensus on the physical phenomena driving aerodynamic instabilities in rotating equipment, and consequently their modeling, is still lacking. Therefore, these estimates can only be used for the selection of the most conservative $k_{xy}$ for preliminary design purposes. Nevertheless, a full characterization of the actual destabilizing effect of the impeller would require at least data obtained with unsteady RANS simulations (Lerche et al., 2013; Pan et al., 2020), and preferably experimental verification on a fully instrumented system.

Consequently, the largest computed value of $|k_{xy}^{\mathrm{aero}}| = |k_{yx}^{\mathrm{aero}}| = 6.25 \times 10^4$ Nm$^{-1}$ is used in analysis of the lateral vibrations documented in the following. Notably, these terms of the stiffness matrix are assumed of equal magnitude and opposite sign, and are thus source of dynamic instability for the shaft-train. Subsequently, a parametric analysis as suggested in the API 617 norm, is conducted to assess system stability throughout the operating range of the machine.

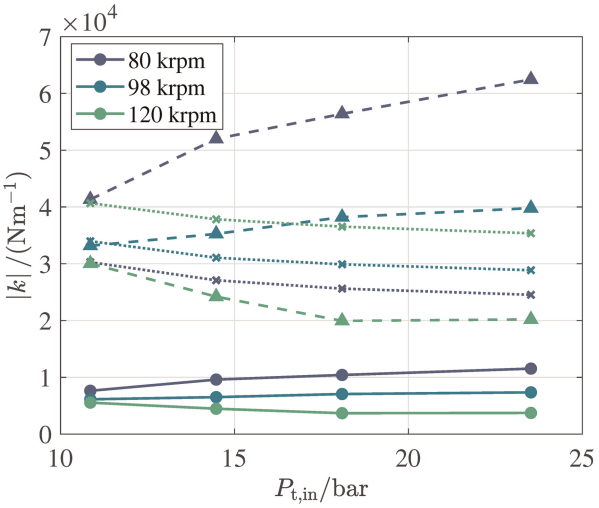


Figure 14. Cross-coupled stiffness coefficient $k_{xy}$ computed using the Wachel method of API 617 (solid lines), the modified Wachel formula for siloxane MM (dashed lines) and the numerical correlation of Moore & Ransom (dotted lines) as a function of the stage inlet total pressure for three different rotational speeds.

## Rotordynamic analysis

The dynamics of the turbine assembly has been investigated by means of a finite element rotordynamic beam model. The model includes those of the shaft train, of the REB cartridge accounting for the SFD characteristics, of the pocket gas seal and of the aerodynamic forcing of the turbine wheel. The graphical representation of the resulting rotordynamic model, made of finite beam elements, is schematically shown in Figure 15, together with the non-rotating cartridge outer ring. The rotating parts include the coupling hub and flange, the bearing lock-nut, the cartridge inner ring, the impeller and the ogive. The presence of a coupling shaft – used to direct-drive a high-speed generator attached to the coupling hub D illustrated in Figure 5 – has been modeled by adding its mass and inertia as lumped parameters on the second element from the left in Figure 15.

The lateral vibrations of the structure are described by the linearized system of equations

$$[M]\ddot{\boldsymbol{x}} + ([C] + \Omega[G])\dot{\boldsymbol{x}} + [K]\boldsymbol{x} = \boldsymbol{F}, \tag{5}$$

where $[M]$, $[C]$, $[G]$ and $[K]$ are respectively the mass, damping, gyroscopic, and the stiffness matrix, while F is a vector representing the synchronous force acting on the rotor center of gravity due to the presence of residual unbalance calculated according to the ISO 1940-1 (ISO, 2003). The unbalance force appears as a result of a relative shift between the rotor center of gravity and the axis of rotation, commonly caused by geometrical tolerances and material imperfections.

The dynamics of the REB is modeled through linearized coefficients using the classical stiffness and damping matrices

$$[K]^{\mathrm{REB}} = \begin{bmatrix} k_{xx}^{\mathrm{REB}} & 0 \\ 0 & k_{yy}^{\mathrm{REB}} \end{bmatrix}, \quad [C]^{\mathrm{REB}} = \begin{bmatrix} c_{xx}^{\mathrm{REB}} & 0 \\ 0 & c_{xx}^{\mathrm{REB}} \end{bmatrix}.$$

$[K]^{\mathrm{REB}}$ and $[C]^{\mathrm{REB}}$ are diagonal matrices because the stiffness and damping cross-terms are negligible. The values of direct stiffness reported in Table 5 were obtained by averaging the stiffness estimated using Hertz contact theory as a function of the radial and axial loads on the bearings, which changed with the rotational speed. A value for the direct damping terms was assumed considering a bearing of similar size, with comparable lubrication characteristics.

The effect of the squeeze-film-damper is considered by introducing a stiffness and a damping matrix with non-null direct terms and null cross-coupled terms $[C]^{\mathrm{SFD}}$ and $[K]^{\mathrm{SFD}}$. Direct terms vary as a function of the rotational speed, and were evaluated by means of the Reynolds model (Equation 1). Instead, the effect of the gas

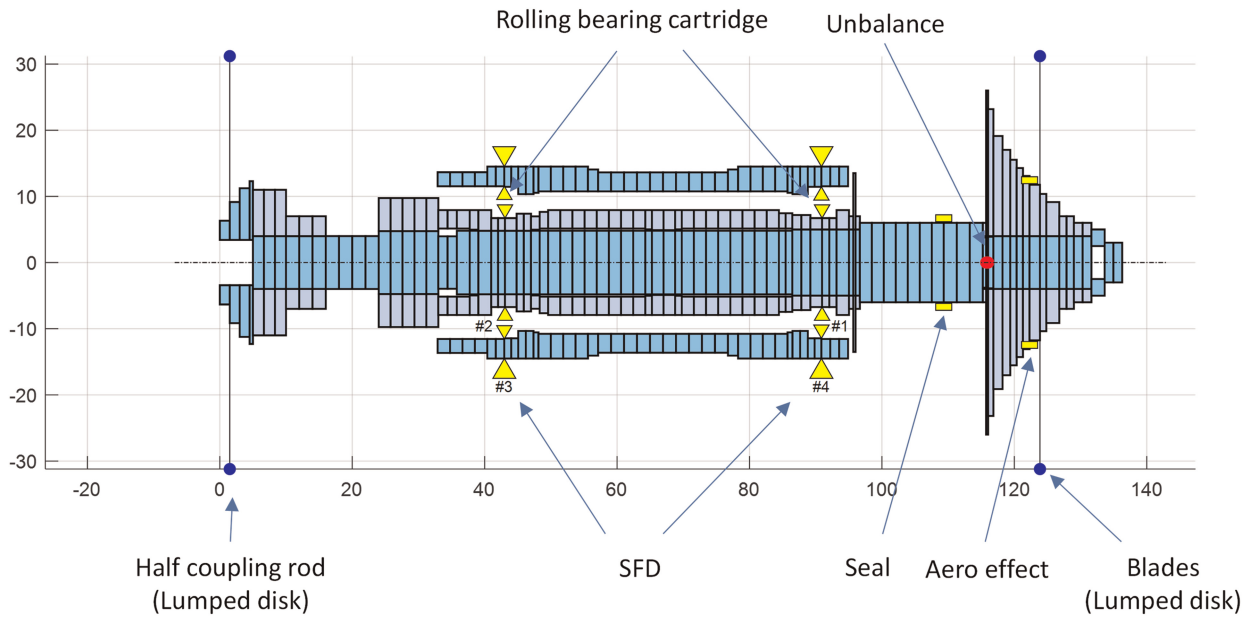


Figure 15. Schematic graphical representation of the rotordynamic model showing the mass distribution of the rotor discretized using disks. The locations where the most important rotordynamic coefficients have been applied as lumped parameters are shown by means of yellow arrowheads. These include the REB stiffness, the SFD damping, the PGS stiffness and damping and the impeller FSI stiffness. The residual unbalance computed as per ISO1940-1 standard is indicated by the red dot, while the coupling disk and the impeller blades lumped masses are indicated by the blue dots. *x*- and *y*- axes allow to evaluate the dimensions in mm of the rotor.

seal is included by means of a stiffness matrix, namely $[K]^{\mathrm{PGS}}$, with equal direct terms of same sign and cross-terms with the same magnitude and opposite sign. The aerodynamic forces exerted by the impeller on the machine shroud are considered by introducing the stiffness matrix $[K]^{\mathrm{aero}}$ with non-zero cross-terms and null direct terms

$$[C]^{\mathrm{SFD}} = \begin{bmatrix} c_{xx}^{\mathrm{SFD}} & 0 \\ 0 & c_{yy}^{\mathrm{SFD}} \end{bmatrix}, \quad [K]^{\mathrm{SFD}} = \begin{bmatrix} k_{xx}^{\mathrm{SFD}} & 0 \\ 0 & k_{yy}^{\mathrm{SFD}} \end{bmatrix}, \quad [K]^{\mathrm{PGS}} = \begin{bmatrix} k_{xx}^{\mathrm{PGS}} & k_{xy}^{\mathrm{PGS}} \\ -k_{xy}^{\mathrm{PGS}} & k_{yy}^{\mathrm{PGS}} \end{bmatrix}, \quad [K]^{\mathrm{aero}} = \begin{bmatrix} 0 & k_{xy}^{\mathrm{aero}} \\ -k_{xy}^{\mathrm{aero}} & 0 \end{bmatrix}.$$

The result of the eigenfrequency analysis as a function of the rotational speed is reported in the Campbell diagram of Figure 16. Fundamental and first harmonic critical speeds, hence the excitation frequencies at which the modes damped natural frequencies cross the 1× and the 2× lines in Figure 16, have been reported in Table 6 along with the corresponding damping factors in the range of rotor speeds going from 20 krpm up to 120 krpm. The mode shapes at each critical speed are shown in Figure 17, where the first 2 mode shapes are mainly rigid modes of the shaft and cartridge relative movement, whereas modes 3–7 are also caused by the bending of the shaft.

Table 5. Constant direct stiffness and damping coefficients used in the rotordynamics calculation.

| Location | $k_{xx}^{\mathrm{REB}}/(\mathrm{Nm}^{-1})$ | $c_{xx}^{\mathrm{REB}}/(\mathrm{Nsm}^{-1})$ |
|---|---|---|
| Impeller side | $50 \cdot 10^6$ | 100 |
| coupling side | $12 \cdot 10^6$ | 100 |

The stiffness was computed using Hertz contact theory and the value reported is the average throughout the range of rotational speed investigated. It was assumed $k_{yy}^{\mathrm{REB}} = k_{xx}^{\mathrm{REB}}$ and $c_{yy}^{\mathrm{REB}} = c_{xx}^{\mathrm{REB}}$.

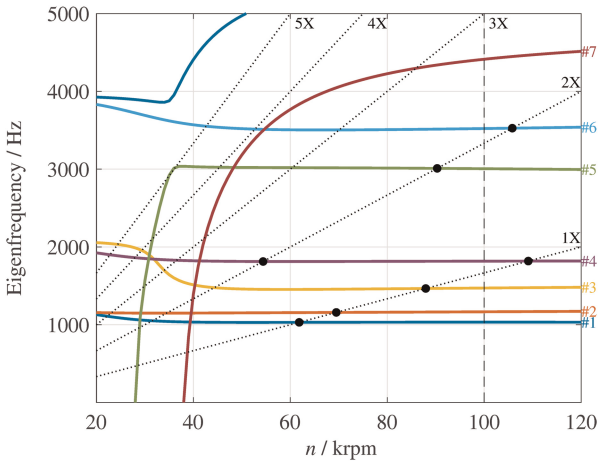


Figure 16. Campbell diagram of the ORCHID turbine rotor. The solid lines indicate the damped natural frequencies associated to each vibration mode up to 5,000 Hz. Dotted oblique lines represent synchronous and super-synchronous excitation frequencies with respect to the shaft speed. Black dots represent critical speed crossings, occurring if the excitation frequency matches the damped natural frequency of any of the modes. Only intersections involving the 1× and 2× shaft excitations are considered for this preliminary analysis.

The coloured bands shown in the Campbell diagram of Figure 18 illustrate the range of variation of the eigenfrequency of each vibrating mode for variations of $k_{xx}^{\mathrm{REB}} \in \pm 30\%$ of the nominal value. The eigenfrequency of mode 7 is significantly affected by the bearing stiffness, while that of the other vibrating modes is almost unaltered.

The rotor is composed of many parts stacked together for construction simplicity. If the shaft vibrates under the action of a bending mode, micro-sliding in the circumferential direction of radially fitted parts can occur. This phenomenon, called internal damping, is a possible source of instability if the machine operates largely above the first critical bending speed. The current analysis shows that the machine operates in a sub-synchronous regime concerning modes 5 and 6 (first bending modes) at the nominal speed of 100 krpm. As a consequence, internal damping was neglected in this investigation. Super-resonance conditions could only occur for large changes in roller bearing stiffness, however Figure 18 shows that the natural frequencies of these modes are unaffected by $k_{xx}^{\mathrm{REB}}$.

The stability of the rotor was investigated by evaluating the damping factor $h$ of each vibrating mode at the nominal rotational speed. The damping factor is defined as $h = -\mathrm{Re}(\lambda)/|\lambda|$, where $\lambda$ is the vector of the

Table 6. Critical speed and damping ratio of several modes crossing the 1× and 2× shaft excitation frequency.

| Mode # | Critical speed/krpm | Damping ratio $h$ |
|---|---|---|
| 1 (1×) | 61.8 | 0.060 |
| 2 (1×) | 69.5 | 0.032 |
| 3 (1×) | 88.9 | 0.096 |
| 4 (1×) | 109.1 | 0.030 |
| 4 (2×) | 54.4 | 0.052 |
| 5 (2×) | 90.3 | 0.067 |
| 6 (2×) | 105.8 | 0.045 |

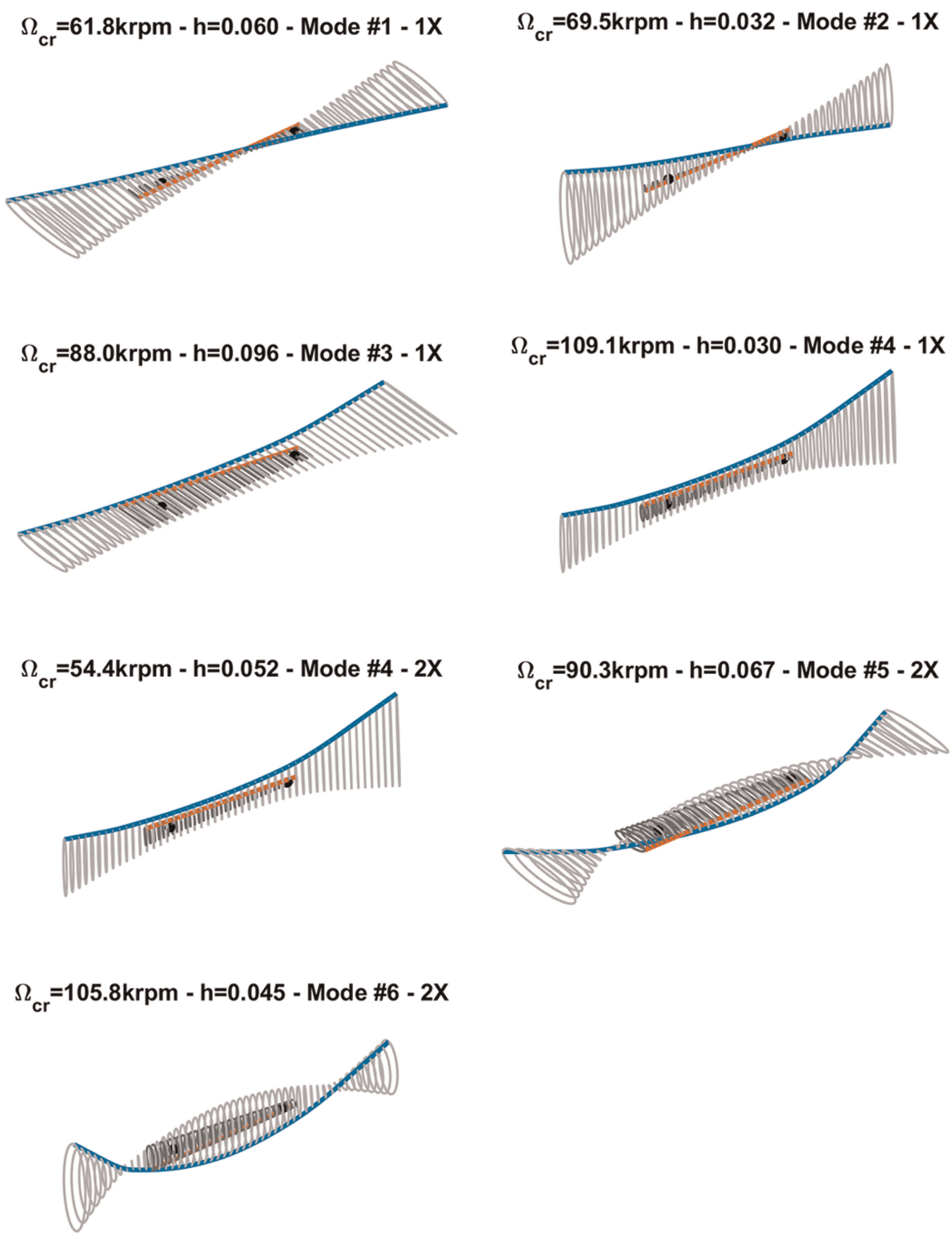


Figure 17. Mode shapes at the critical speeds reported in Table 6. The solid blue line represents the shaft center line, while the red line indicates the cartridge outer ring center line. Orbits described by the two center lines are represented in grey.

eigenvalues of the system described by Equation 5. If this is negative, the system is unstable (Bachschmid et al., 2008). Following API 617, the stability analysis has been performed by progressively varying the magnitude of the aerodynamic stiffness cross-terms $k_{xy}^{\text{aero}}$ and $k_{xy}^{\text{PGS}}$, by multiplying them by a factor $\eta \in (1, \ldots, 10)$. The effect of increasing $\eta$ on the system eigenfrequencies is shown in the left Campbell diagram of Figure 19, while the system stability map is shown in the right plot, which illustrates the change in damping factor $h$ associated to each mode. Shaded bands indicate the eigenfrequency variation interval corresponding to variations of $k_{xx}^{\text{REB}} \in \pm 30\%$ of the nominal value. The eigenfrequency of each of the modes is almost unaffected by the change of $\eta$. Mode #1 becomes unstable ($h < 0$) for large values of $\eta$. However, since mode #1 is a rigid movement between the shaft and the cartridge, the instability is not deemed critical.

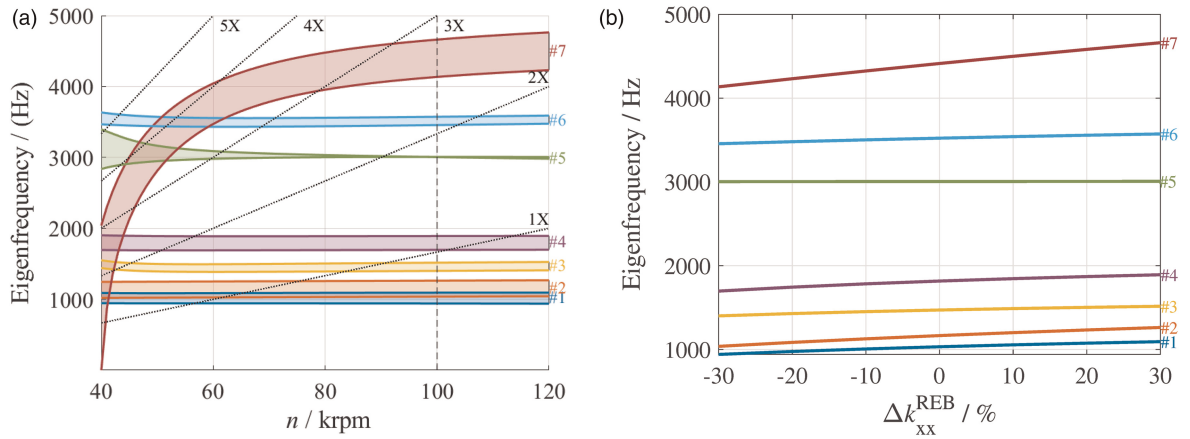


Figure 18. (a) Campbell diagram of the rotor system as a function of shaft speed. The colored bands indicate the impact of a varying bearing stiffness in an interval ±30% of the nominal value given by Hertz contact theory. (b) System natural frequencies as a function of the bearing stiffness at the nominal speed of 100 krpm.

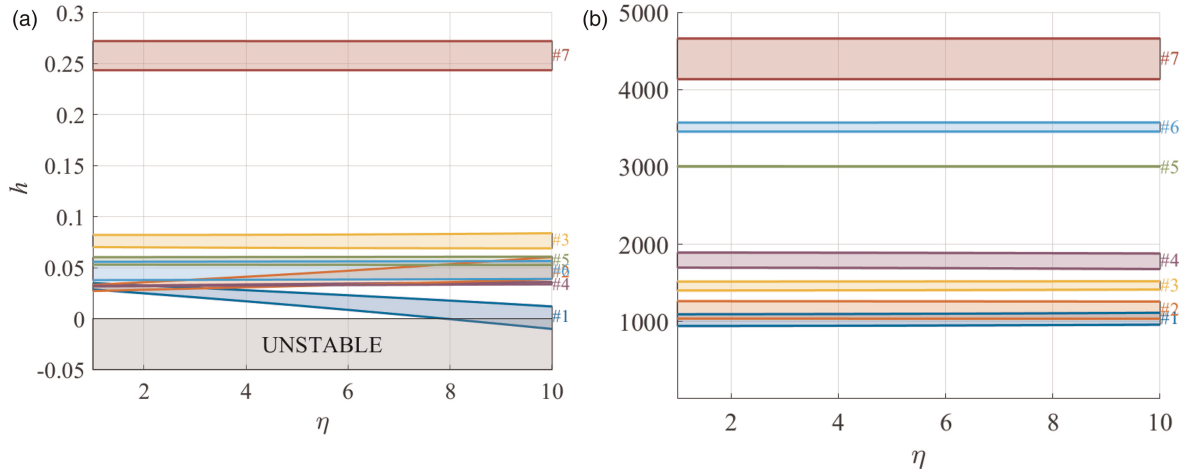


Figure 19. (a) System natural frequencies and (b) stability map as a function of the multiplying coefficient $\eta$ of stiffness cross-terms at $n = 100$ krpm. The colored bands indicate the impact of a varying bearing stiffness in an interval ±30% of the nominal value given by Hertz contact theory.

## Conclusion

This paper documents the mechanical design and rotordynamic analysis of the high-speed rotor of the ORCHID turbine. The bearing unit selected to support the overhanging turbine wheel and coupling hub flange is a turbocharger ball bearing assembly. The component features an external cartridge that acts as a squeeze film damper, providing damping to the shaft-train. The damping coefficients of the cartridge were computed numerically throughout the entire operating range of the machine, considering a nominal radial clearance of 50 µm with the turbine housing. Results obtained by solving the Reynolds equation for the oil-film complemented by a linearized cavitation model showed that rotor damping deteriorates at increasing rotational speed due to the increasingly larger portion of oil-film that undergoes cavitation. Moreover, the cartridge acts as a spring, thus introducing additional stiffness which is largely dependent on the dynamic eccentricity and static eccentricity of the rotor.

A pocket gas seal was designed in-house to limit the leakage flow rate of working fluid to the bearings housing. The leakage massflow rate calculated by means of RANS simulations was compared to the value obtained with an empirical method commonly employed for the sealing design of gas turbines. Predictions from the CFD and the empirical method were in close agreement, showing that such an empirical correlation is applicable for the estimation of the leakage mass flow rate through pocket gas seals of high-speed ORC turbines.

Moreover, RANS simulations were carried out to compute the stiffness and damping coefficients of the pocket gas seal. The results show that this type of gas seal leads to comparatively small direct and cross-coupled stiffness terms, which were included in the rotordynamic analysis to evaluate the impact of the seal on system stability. Conversely, the damping provided by the pocket gas seal is negligible compared to that of the squeeze film damper, being about 5 to 6 orders of magnitude lower.

The analysis considers also the presence of destabilizing aerodynamic forces due to the fluid-structure interaction between the unshrouded impeller and the casing. Predictions obtained with the Wachel and the Moore & Ransom model have been compared, showing reasonable agreement between the force magnitudes for preliminary calculations. Higher fidelity methods such as unsteady RANS simulations should however be used for a more accurate assessment.

The lateral vibration analysis of the first 7 mode shapes reveals the presence of rigid modes (1 and 2) and flexible modes (from 3 to 7). A sensitivity analysis was carried out to investigate the impact of modeling assumptions on the results of the rotordynamic analysis. In particular, mode #7 exhibits a large sensitivity to variations of $\pm 30\%$ of the bearings stiffness coefficient, which was computed using the Hertz contact theory. Despite this, no critical speed with the 1× and 2× shaft speed excitation frequencies is observed for this mode within the nominal operating range of the rotor. Modes #5 and 6 instead show a weak dependence on the bearing stiffness, but do have critical speeds of 2× shaft speed excitation frequency in the range $80-120$ krpm.

Finally, the stability of the rotor was assessed by investigating the change in damping ratio $h$ of each mode shape for increasing values of the cross-coupled stiffness coefficients associated to the impeller-shroud aerodynamic force, and of the PGS stiffness coefficients. The analysis highlights that mode #1 becomes unstable only if values of the cross-coupled stiffness coefficients are about one order of magnitude larger than those estimated in this study. Nevertheless, since the computation of the destabilizing stiffness term (especially the impeller-shroud force) is subject to large uncertainty, the analysis presented here is purely indicative of a worst case scenario and further investigations are necessary to properly evaluate its impact on system stability.

Future work will be devoted to the testing of the rotor, properly instrumented with embedded sensors to measure the vibration amplitude at different rotational speeds, and to characterizing its transient dynamics. Moreover, more in depth numerical investigations using higher fidelity models, such as full-annulus unsteady RANS simulations, are considered necessary to obtain further insight about the destabilizing nature of the cross-coupled stiffness coefficients resulting from the impeller secondary flows.

## Funding sources

Applied and Engineering Sciences Division (TTW) of the Dutch Organization for Scientific Research (NWO), Grant No. 17906.

## Competing interests

Matteo Majer declares that he has no conflict of interest. Steven Chatterton declares that he has no conflict of interest. Ludovico Dassi declares that he has no conflict of interest. Edoardo Gheller declares that he has no conflict of interest. Paolo Emilio Lino Maria Pennacchi declares that he has no conflict of interest. Piero Colonna declares that he has no conflict of interest. Matteo Pini declares that he has no conflict of interest.

## References

Alford J. S. (1965). Protecting turbomachinery from self-excited rotor whirl. *Journal of Engineering for Power*. 87 (4): 333–343. https://doi.org/10.1115/1.3678270.

Ansys Inc. (2021). Academic Research Fluent, Release 21.0.

Ansys Inc. (2022). Academic Research CFX, Release 22.0.

API (2002). API 617. Axial and centrifugal compressors and expander-compressors for petroleum, chemical and gas industry, 7th ed. Technical report, American Petroleum Institute.

Bachschmid N., Pennacchi P., and Vania A. (2008). Steam-whirl analysis in a high pressure cylinder of a turbo generator. *Mechanical Systems and Signal Processing*. 22 (1): 121–132. https://doi.org/10.1016/j.ymssp.2007.04.005.

Barth T. and Jespersen D. (1989). The design and application of upwind schemes on unstructured meshes. *27th Aerospace Sciences Meeting*. AIAA. https://doi.org/10.2514/6.1989-366,

Bella F. D., Cho J.-K., Kwon J.-S., and Gyun Jeong H. (2015). Development and testing of a 250 kWe ORC system using an integrated axial turbine and high speed generator for 3.7 bar, a condensing steam. In Proceedings of the 3rc International Seminar on ORC Power Systems.

Blunk H. and Seibel A. (2023). Design guidelines for metal binder jetting. *Progress in Additive Manufacturing*. 9: 725–732. https://doi.org/10.1007/s40964-023-00475-y.

Calnetix Technologies (n.d.). https://www.calnetix.com/.

Cappiello A. and Tuccillo R. (2021). Design parameter influence on losses and downstream flow field uniformity in supersonic ORC radial-inflow turbine stators. *International Journal of Turbomachinery, Propulsion and Power*. 6 (3). https://doi.org/10.3390/ijtpp6030038.

Cappiello A., Majer M., Tuccillo R., and Pini M. (2022). On the influence of stator-rotor radial gap size on the fluid-dynamic performance of mini-ORC supersonic turbines. In Proceedings of the ASME Turbo Expo 2022: Turbomachinery Technical Conference and Exposition, Vol. 10B, p. V10BT35A015. https://doi.org/10.1115/GT2022-83309.

Childs D., Elrod D., and Hale K. (1989). Annular honeycomb seals: test results for leakage and rotordynamic coefficients; comparisons to labyrinth and smooth configurations. *Journal of Tribology*. 111: 293–300. https://doi.org/10.1115/1.3261911.

Climeon (n.d.). https://climeon.com/.

Colonna P., Casati E., Trapp C., Mathijssen T., Larjola J., et al. (2015). Organic Rankine cycle power systems: from the concept to current technology, applications, and an outlook to the future. *Journal of Engineering for Gas Turbines and Power*. 137 (10): 100801–100819. https://doi.org/10.1115/1.4029884.

Concepts NREC (n.d.). https://www.conceptsnrec.com/.

Delgado A. and San Andres L. A. (2010). Model for improved prediction of force coefficients in grooved squeeze-film-dampers and oil seal rings. *Journal of Tribology*. 132 (3): 032202. https://doi.org/10.1115/1.4001459.

Delgado A., San Andrés L., Yang J., and Thiele J. (2022). Experimental force coefficients for a fully-partitioned pocket damper seal and comparison to other two seal types. In Proceedings of the ASME Turbo Expo 2022: Turbomachinery Technical Conference and Exposition, Vol. 8A, p. V08AT22A020. https://doi.org/10.1115/1.4056347.

De Servi C. M., Burigana M., Pini M., and Colonna P. (2019). Design method and performance prediction for radial-inflow turbines of high-temperature mini-organic Rankine cycle power systems. *Journal of Engineering for Gas Turbines and Power*. 141 (9): 091021. https://doi.org/10.1115/1.4043973.

Egli A. (1935). The leakage of steam through labyrinth seals. *Journal of Fluids Engineering*. 57: 115–122.

Enogia (n.d.). https://enogia.com/.

Ertas B. H., Delgado A., and Vannini G. (2012). Rotordynamic force coefficients for three types of annular gas seals with inlet preswirl and high differential pressure ratio. *Journal of Engineering for Gas Turbines and Power*. 134 (4): 042503. https://doi.org/10.1115/1.4004537.

Ewald A. and Schlattmann J. (2018). Design guidelines for laser metal deposition of lightweight structures. *Journal of Laser Applications*. 30 (3): 032309. https://doi.org/10.2351/1.5040612.

Fan T. and Behdinan K. (2017). The evaluation of linear complementarity problem method in modeling the fluid cavitation for squeeze film damper with off-centered whirling motion. *Lubricants*. 5 (4). https://doi.org/10.3390/lubricants5040046.

Forsthoffer W. E. (2011) Dry gas seal best practices. In: Forsthoffer's best practice handbook for rotating machinery. Butterworth-Heinemann, Boston, 501–524.

Gheller E., Chatterton S., Vania A., and Pennacchi P. (2022). Squeeze film damper modeling: a comprehensive approach. *Machines*. 10 (9). https://doi.org/10.3390/machines10090781.

Harinck J., Pasquale D., Pecnik R., Buijtenen J. V., and Colonna P. (2013). Performance improvement of a radial organic Rankine cycle turbine by means of automated computational fluid dynamic design. *Proceedings of the Institution of Mechanical Engineers, Part A: Journal of Power and Energy*. 227: 637–645. https://doi.org/10.1177/0957650913499565.

Head A. J. (2021). Novel experiments for the investigation of non-ideal compressible fluid dynamics. PhD thesis, TU Delft.

Huber M. L., Lemmon E. W., Bell I., and McLinden M. O. (2022). The NIST REFPROP database for highly accurate properties of industrially important fluids.

ISO (2003). ISO 1940-1. mechanical vibration — balance quality requirements for rotors in a constant (rigid) state — part 1: specification and verification of balance tolerances. Technical report, International Organization for Standardization.

Kang S. H. (2016). Design and preliminary tests of ORC (organic Rankine cycle) with two-stage radial turbine. *Energy*. 96: 142–154. https://doi.org/10.1016/j.energy.2015.09.040.

Klonowicz P., Borsukiewicz-Gozdur A., Hanausek P., Kryłłowicz W., and Brüggemann D. (2014). Design and performance measurements of an organic vapour turbine. *Applied Thermal Engineering*. 63 (1): 297–303. https://doi.org/10.1016/j.applthermaleng.2013.11.018.

Lerche A. H., Musgrove G. O., Moore J. J., Kulhanek C. D., and Nordwall G. (2013). Rotordynamic force prediction of an unshrouded radial inflow turbine using computational fluid dynamics. In Proceedings of the ASME Turbo Expo 2013: Turbine Technical Conference and Exposition, Vol. 7A, p. V07AT29A015. https://doi.org/10.1115/GT2013-95137.

Ludwig L. P. (1980). Gas path sealing in turbine engines. *Tribology Transactions*. 23: 1–22.

Moore J. J., Ransom D. L., and Viana F. (2010). Rotordynamic force prediction of centrifugal compressor impellers using computational fluid dynamics. *Journal of Engineering for Gas Turbines and Power*. 133 (4): 042504. https://doi.org/10.1115/1.2900958.

Nguyen-Schäfer H. (2012.) Rotordynamics of automotive turbochargers. Heidelberg: Springer Berlin.

Orcan Energy (n.d.). https://www.orcan-energy.com/.

Pan Y., Yuan Q., Huang G., Gu J., Li P., and Zhu G. (2020). Numerical investigations on the blade tip clearance excitation forces in an unshrouded turbine. *Applied Sciences*. 10: 1532. https://doi.org/10.3390/app10041532.

Rank (n.d.). https://www.rank-{ORC}.com/.

Rosset K., Pajot O., and Schiffmann J. (2021). Experimental investigation of a small-scale organic Rankine cycle turbo-generator supported on gas-lubricated bearings. *Journal of Engineering for Gas Turbines and Power*. 143 (5): 051015. https://doi.org/10.1115/1.4049988.

San Andres L. (2023). A review of turbine and compressor aerodynamic forces in turbomachinery. *Lubricants*. 11 (1). https://doi.org/10.3390/lubricants11010026.

San Andres L. and Jeung S. H. (2016). Orbit-model force coefficients for fluid film bearings: a step beyond linearization. *Journal of Engineering for Gas Turbines and Power*. 138 (2): 022502. https://doi.org/10.1115/1.4031237.

San Andres L. A. and Vance J. M. (1987). Effects of fluid inertia on finite-length squeeze-film dampers. *ASLE Transactions*. 30: 384–393. https://doi.org/10.1080/05698198708981771.

Schweitzer F. and Adleff K. (2006). Rolling bearings in turbocharger applications. *MTZ Worldwide*. 67: 16–19. https://doi.org/10.1007/BF03227869.

Seume J. R., Peters M., and Kunte H. (2017). Design and test of a 10 kW ORC supersonic turbine generator. *Journal of Physics: Conference Series*. 821: 012023. https://doi.org/10.1088/1742-6596/821/1/012023.

Triogen (n.d.). https://triogen.nl/.

Uusitalo A., Turunen-Saaresti T., Honkatukia J., and Dhanasegaran R. (2020). Experimental study of small scale and high expansion ratio ORC for recovering high temperature waste heat. *Energy*. 208: 118321. https://doi.org/10.1016/j.energy.2020.118321.

Vance J. (1998). Rotordynamics of turbomachinery. New York: John Wiley and Sons.

Wachel J. and von Nimitz W. (1981). Ensuring the reliability of offshore gas compression systems. *Journal of Petroleum Technology*. 33 (11): 2252–2260. https://doi.org/10.2118/10591-PA.

Weiß A. A. (2018). Experimental characterization and comparison of an axial and a cantilever micro-turbine for small-scale organic Rankine cycle. *Applied Thermal Engineering*. 140: 235–244. https://doi.org/10.1016/j.applthermaleng.2018.05.033.

Yuksek E. L. and Mirmobin P. (2015). Electricity generation from large marine vessel engine jacket water heat. In ASME 2015 9th International Conference on Energy Sustainability, ES 2015, collocated with the ASME 2015 Power Conference, the ASME 2015 13th International Conference on Fuel Cell Science, Engineering and Technology, and the ASME 2015 Nuclear Forum 2. https://doi.org/10.1115/ES2015-49226.

Zeidan F. Y. and Vance J. M. (1990). Cavitation regimes in squeeze-film-dampers and their effect on the pressure distribution. *Tribology Transactions*. 33 (3): 447–453. https://doi.org/10.1080/10402009008981975.

Zuccato Energy (n.d.). https://zuccatoenergy.com.